Crystallization behavior of silica–calcium phosphate biocomposites: XRD and FTIR studies

C. Q. NING[1], Y. GREISH[2], A. EL-GHANNAM[1]*
[1]Center for Biomedical Engineering, University of Kentucky, Lexington, KY 40506, USA
Email: arelgh2@uky.edu
[2]Materials Research Institute, Pennsylvania State University, University Park, PA 16802, USA

Silica and calcium phosphates (CaP) are the most important ingredients in bioactive materials that bond to bone and enhance bone tissue formation. In this study, silica–calcium phosphate (SiO_2–CaP) composites were developed by powder metallurgy method, using silica (SiO_2) and anhydrous dicalcium phosphate ($CaHPO_4$) powders (CaP) in the ratios (wt %): 20/80, 40/60, 60/40 and 80/20. The effects of temperature and chemical composition on crystallization and phase transformation of the SiO_2–CaP composites were evaluated by XRD and FTIR. Thermal treatment of the starting material suggested that $CaHPO_4$ transforms into: γ-$Ca_2P_2O_7$ at 800 °C; β-$Ca_2P_2O_7$ at 1000 °C and α-$Ca_2P_2O_7$ at 1200 °C. On the other hand, β-quartz was the only detected phase after thermal treatment of silica in the temperature range 800–1200 °C. For all SiO_2–CaP composites, SiO_2 and CaP did not modify the crystallization behavior of each other when sintered in the temperature range 800–1000 °C. However, at 1200 °C, CaP promoted the transformation of β-quartz into α-cristobalite. Moreover, SiO_2 stabilized β-$Ca_2P_2O_7$. The modifications in the crystallization behavior were related to ion substitution and formation of solid solutions.

1. Introduction

Bioactive calcium phosphate ceramics such as hydroxyapatite ($Ca_{10}(PO_4)_6(OH)_2$) (HA) and tricalcium phosphate ($Ca_3(PO_4)_2$) (TCP) have been widely used as bone graft materials. These materials have chemical composition and crystalline structure similar to the mineral phase of bone. Therefore, they bond to bone and enhance bone formation [1–5]. However, data in the literature indicated that HA ceramics have limited bioactivity and resorbability [6]. On the other hand, TCP is characterized by high resorbability rate after implantation which elicits immunological responses [7].

Silica-based bioactive glasses are characterized by superior bioactivity than calcium phosphate ceramics [8]. Previous reports have demonstrated that the silicon plays an important role in the surface bioactivity of bioactive glasses [9–12]. In biological fluids, ion exchange at the glass/solution interface results in the formation of a silica-rich layer that nucleates the precipitation of a calcium phosphate layer similar to the mineral phase of bone on the glass surface [1, 10]. The formation of this layer is a prerequisite for bone bonding. The importance of silicon as essential nutrition element for bone development has also been reported. Electron microprobe studies by Carlisle have shown that silicon was localized in active growth areas of the young bone of mice and rats, which indicates that silicon plays an important role in bone formation and calcification [13].

Attempts to improve the bioactivity of HA ceramic included the modification of its chemical composition by silica [14–20]. *In vitro* studies by Gibson *et al.* [21] proved that the incorporation of silicon into the crystal structure of pure HA enhanced the osteoblast-like cell activity. The enhanced bioactivity was attributed to the formation of a poorly crystallized surface apatite layer on silica-substituted HA. Moreover, *in vivo* studies showed enhanced bioactivity and resorbability for silica-substituted HA [22, 23]. The enhanced bioactivity of silica-substituted HA has been attributed to the enhanced material dissolution (resorbability) *in vivo*. It should be noted that the goal of these previous studies was to incorporate silica in HA without altering its crystalline structure. Therefore, the maximum silica content that can be incorporated in HA without decomposing its structure was 3.32% [20]. In this study, we synthesize silica–calcium phosphate (SiO_2–CaP) composites by powder metallurgy method. We vary the silica content from 20 to 80 wt % and evaluate the effects of sintering temperature and chemical composition on crystallization and phase transformation of the SiO_2–CaP composite.

2. Materials and methods

2.1. Preparation of SiO_2–CaP composites

Highly pure SiO_2 (99%) (Sigma-Aldrich Co.) and $CaHPO_4$ (98–105%) (Sigma-Aldrich Co.) powders

*Author to whom all correspondence should be addressed.

TABLE I Composition design of the SiO_2–CaP composites

Composite code	Composition	
	$CaHPO_4$ (wt %)	SiO_2 (wt %)
CaP	100	0
20Si	80	20
40Si	60	40
60Si	40	60
80Si	20	80
SiO_2	0	100

were used as the starting materials. Table I shows the various compositions used in this study. The original powders were mixed in polyethylene bottles on a rolling mixer for 20 h. The mixtures were then uniaxially pressed into discs (13 mm diameter × 2 mm height) under a pressure of 100 MPa. The pressed discs were then fired separately at 800, 1000 or 1200 °C for 1 h in air at a ramp rate of 20 °C/min. Samples were ground into powders for X-ray diffraction (XRD) and Fourier transform infrared (FTIR) analyses.

2.2. X-ray diffraction

The phase composition of the SiO_2–CaP composites was determined on a Rigaku D/Max X-ray diffractometer (Japan). Cu Kα radiation was used at the operating condition of 40 kV and 20 mA. The XRD data were collected over the 2θ range of 20–80° with a step size of 0.02°. Identification of phases was achieved by comparing the diffraction patterns of the composites with the standard PDF cards.

2.3. FTIR spectroscopy

FTIR analyses were conducted on a Thermo Nicolet Nexus 670 spectrometer (WI, USA). Spectra were collected in the diffuse reflectance mode after 200 scans at 4 cm^{-1} resolution. Samples were prepared by mixing powders of the composites with KBr. Pure KBr was used as a background.

3. Results

3.1. XRD

XRD analysis of the original SiO_2 and $CaHPO_4$ powders indicated that they composed of β-quartz and monetite respectively (Fig. 1(a) and (b)). The XRD data of these two samples coincided with the data in the cards (PDF #46-1045) and (PDF #09-0080). Fig. 2(a)–(c) presents the XRD spectra of the starting materials and the SiO_2–CaP composites after thermal treatments at (a) 800 °C, (b) 1000 °C and (c) 1200 °C. Fig. 2(a) showed that, at 800 °C monetite transformed into γ-$Ca_2P_2O_7$ (PDF #17-0499), while β-quartz remained the main silica phase. All compositions of SiO_2–CaP composites consisted of γ-$Ca_2P_2O_7$ and β-quartz, however, as the SiO_2 content increased, the diffraction intensity of γ-$Ca_2P_2O_7$ decreased, and that of β-quartz increased. After sintering at 1000 °C (Fig. 2(b)), XRD showed that γ-$Ca_2P_2O_7$ transformed into β-$Ca_2P_2O_7$ (PDF #09-0346). On the other hand, the main crystal phase of SiO_2 was β-quartz. Both β-quartz and β-$Ca_2P_2O_7$ were the main constituents of all SiO_2–CaP composites sintered at 1000 °C. However, their ratios varied according to the initial chemical composition.

XRD analyses of the sample treated at 1200 °C (Fig. 2(c)) showed that the CaP phases present were dependent on the sample composition. The main phase of silica was β-quartz. However, traces of α-cristobalite (PDF #39-1425) were also detected in pure SiO_2 as indicated by the appearance of a small peak at 21.62°. The signals characteristics of α-cristobalite increased as the calcium phosphate percentage in the SiO_2–CaP composites increased from 0 to 60 wt %. While the calcium phosphate phase of 20Si was in the form of α-$Ca_2P_2O_7$, that of 40Si, 60Si and 80Si was in the form of β-$Ca_2P_2O_7$. In addition, we observed shifts in the values of the interplanar spacing of β-$Ca_2P_2O_7$ and α-cristobalite that formed in the SiO_2–CaP composites. While the main XRD signals of β-$Ca_2P_2O_7$ were slightly shifted to higher 2θ values (compared to PDF card #09-0346) (Fig. 3(a)), those characteristic of α-cristobalite were shifted to lower 2θ values (compared to PDF card #39-1425) (Fig. 3(b)).

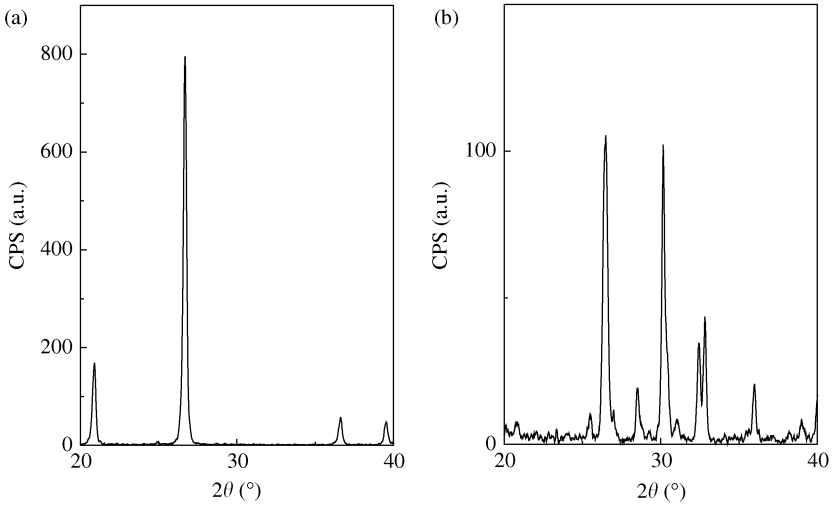

Figure 1 XRD analyses of the starting materials: (a) SiO_2 (β-quartz) and (b) $CaHPO_4$ (monetite).

3.2. FTIR results

The FTIR spectra of the starting materials (SiO_2 and $CaHPO_4$) are shown in Fig. 4(a) and (b) respectively. The assignments of the signals in the spectra of Fig. 4(a) and (b) are shown in Tables II and III respectively. For SiO_2 powder, the bands at 1000–1300 cm^{-1} (including a broad band and two small bands at 1062 and 1160 cm^{-1}) are attributed to the Si–O–Si asymmetric stretching vibrations. The small band at 915 cm^{-1} is due to the vibration of non-bridging oxygens. The doublet at 781 and 800 cm^{-1} is originated from Si–O–Si bending vibrations. The strong band at 695 cm^{-1} is most probably due to the vibrations of six-membered rings [27]. The bands at lower wave numbers, including 418, 477 and 522 cm^{-1} are due to Si–O–Si bending vibrations. Combined with XRD analysis, it is known that the original SiO_2 powder is β-quartz, therefore these bands can be taken as characteristics of β-quartz.

FTIR analysis of $CaHPO_4$ powder (Fig. 4(b)) showed sharp peaks at 1076 and 1134 cm^{-1} and a shoulder at 1170 cm^{-1} which are attributed to the P–O asymmetric stretching mode. The sharp band at 995 cm^{-1} is due to

TABLE II FTIR absorption bands of SiO_2 powder

Wave number (cm^{-1})	Assignments	Ref.
1160	Si–O–Si asymmetric stretching	[26, 28]
1127		
1062		
915	Stretching vibration of	[26]
944	non-bridging oxygens (Si–O^-)	
800	Si–O–Si bending	[27]
781		
695	Six-membered rings	[27]
522	Si–O–Si bending	[26, 28]
477		

TABLE III FTIR absorption bands of $CaHPO_4$ powder

Wave number (cm^{-1})	Assignments	Ref.
1170 (shouler)	P–O asymmetric stretching	[29, 30]
1134		
1076		
995	P–O symmetric stretching	[29]
892	P–O(H) stretching	[29]
583	O–P–O(H) bending	[30]
564		
537		
472	O–P–O bending	[30]
405		

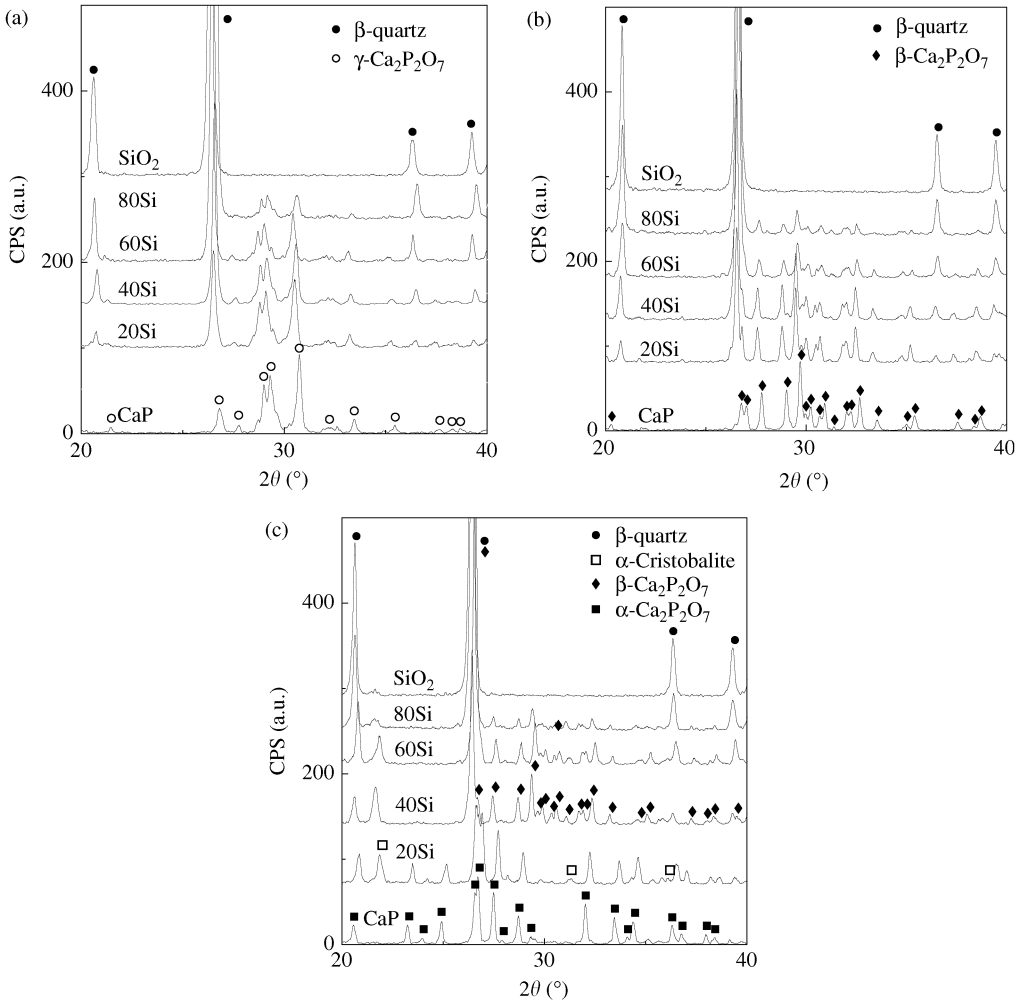

Figure 2 XRD patterns of the SiO_2–CaP composites thermal-treated at different temperatures (a) 800 °C; (b) 1000 °C; (c) 1200 °C. β-quartz was the dominating silica phase at the experimental temperature range of 800–1200 °C. $CaHPO_4$ transformed into γ-$Ca_2P_2O_7$, β-$Ca_2P_2O_7$ and α-$Ca_2P_2O_7$ at 800 °C, 1000 °C and 1200 °C, respectively. At higher temperature (1200 °C), CaP enhanced the transformation of β-quartz to α-cristobalite and silica stabilized β-$Ca_2P_2O_7$. At lower temperatures (800 and 1000 °C) CaP and silica did not modify their corresponding crystallization behavior.

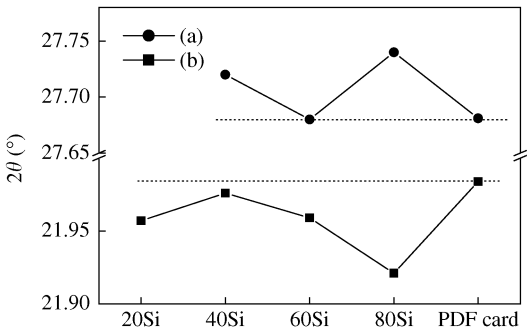

Figure 3 2θ values of (a) (0 0 8) plane of β-$Ca_2P_2O_7$ and (b) (1 0 1) plane of α-cristobalite in the SiO_2–CaP composites thermal-treated at 1200 °C. The 2θ values of α-cristobalite are lower than that in the PDF card of #39-1425; those of (0 0 8) plane of β-$Ca_2P_2O_7$ are higher than that in the PDF card of #09-0346.

the P–O symmetric stretching vibrations. The peak at 877 is due to P–O(H) stretching vibration. The bands at 537, 564 and 583 cm^{-1} belong to the O–P–O(H) bending mode. Other bands at 405 and 472 cm^{-1} are due to the O–P–O bending mode. Combined with XRD analysis, it is known that the original $CaHPO_4$ powder is pure monetite, therefore these bands are characteristics of this phase.

The FTIR spectra of the SiO_2–CaP composites sintered at 800 °C are shown in Fig. 5 and the assignments of the spectra are given in Table IV. The spectra for pure γ-$Ca_2P_2O_7$ showed signals at 451, 498, 536, 567, 585, 610, 720, 954, 1001, 1035, 1087, 1144, 1165, 1187 cm^{-1}; these bands declined as the silica content increased in the SiO_2–CaP composites. On the

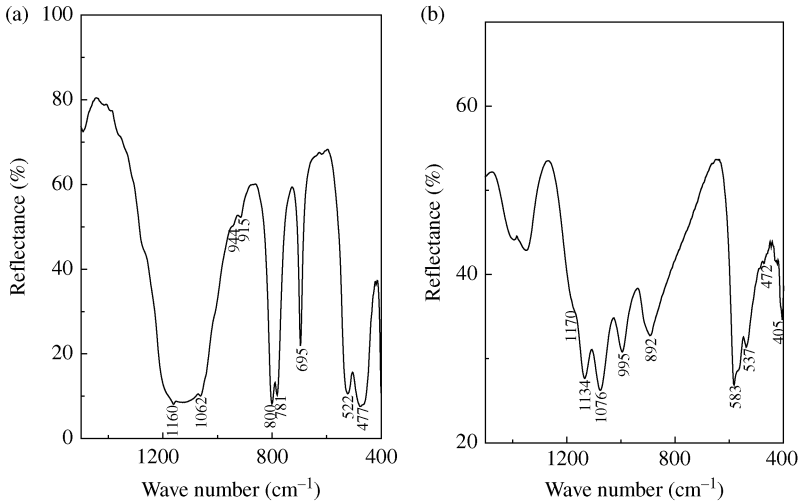

Figure 4 FTIR spectra of the starting material: (a) SiO_2 (β-quartz) and (b) $CaHPO_4$ (monetite).

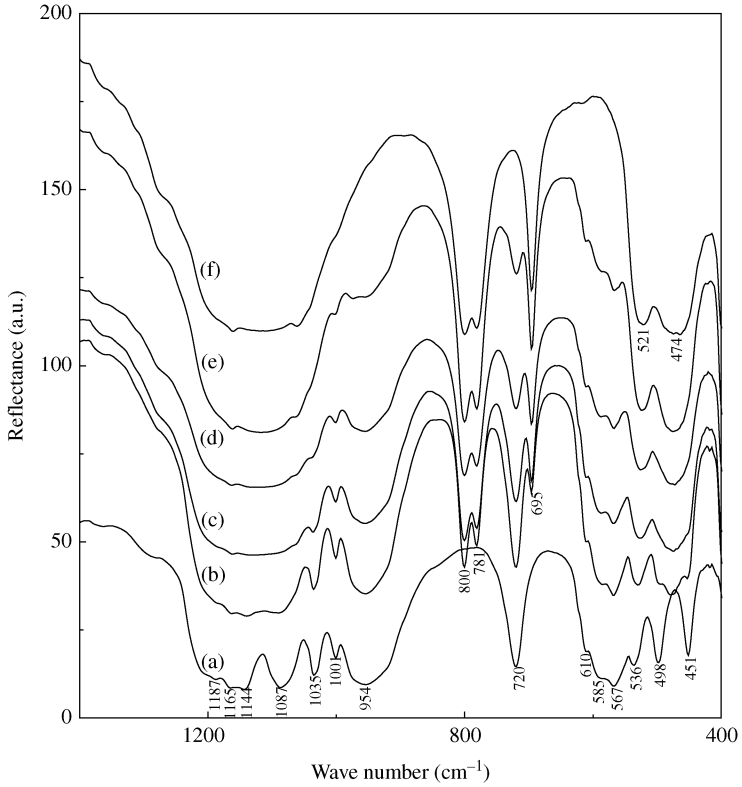

Figure 5 FTIR spectra of the SiO_2–CaP composites thermal-treated at 800 °C, (a) CaP, (b) 20Si, (c) 40Si, (d) 60Si, (e) 80Si, (f) SiO_2. The intensities of the bands for γ-$Ca_2P_2O_7$ at 451, 498, 536, 567, 585, 610, 720, 954, 1001, 1035, 1087, 1144, 1165, 1187 cm^{-1} decreased with increasing silica content, whereas, those of the bands for β-quartz at 474, 521, 695, 781, 800, 1062, 1127, 1161 cm^{-1} increased.

TABLE IV FTIR absorption bands of the SiO_2–CaP composites sintered at 800 °C

Wave number (cm^{-1})						Assignments	Ref.
CaP	20Si	40Si	60Si	80Si	SiO_2		
1187	1187	1178				Asymmetrical terminal P–O stretching mode:	[31]
1165						$\upsilon_{as}PO_3(\gamma\text{-}Ca_2P_2O_7)$	
	1163	1162	1162	1162	1161	Si–O–Si asymmetric stretching	[26, 28]
1144	1140					$\upsilon_{as}PO_3(\gamma\text{-}Ca_2P_2O_7)$	[31]
	1127	1127	1127	1127	1127	Si–O–Si asymmetric stretching	[26, 28]
1087	1090					$\upsilon_{as}PO_3(\gamma\text{-}Ca_2P_2O_7)$	[31, 32]
			1063	1063	1062	Si–O–Si asymmetric stretching	[26, 28]
1035	1035	1036	1036	1003		Symmetrical terminal P–O stretching mode:	[33, 34]
1001	1001		1001			$\upsilon_{s}PO_3(\gamma\text{-}Ca_2P_2O_7)$	
954	954	955	955	955		Asymmetrical bridge P–O stretching mode:	[31, 33]
						$\upsilon_{as}POP$ ($\gamma\text{-}Ca_2P_2O_7$)	
	801	801	800	800	800	Si–O–Si bending	[27]
	782	781	781	781	781		
720	720	720	720	719		Symmetrical bridge P–O stretching mode:	[31, 34]
						$\upsilon_{s}POP$ ($\gamma\text{-}Ca_2P_2O_7$)	
	696	696	696	696	695	Six-membered rings (β-quartz)	[27]
610	610	610	610	610		Asymmetrical terminal P–O bending mode:	[31, 33]
						$\delta_{as}PO_3(\gamma\text{-}Ca_2P_2O_7)$	
585	585	587	587	587		Symmetrical terminal P–O bending mode:	[31, 32]
						$\delta_{s}PO_3(\gamma\text{-}Ca_2P_2O_7)$	
567	568	568	567	567		$\delta_{as}PO_3$	[31, 32]
536							
	530	527	526	523	521	Si–O–Si bending	[26, 28]
498	494					$\delta_{s}PO_3$	[33, 34]
	479	475	473	472	474	Si–O–Si bending	[26, 28]
451	453					$\delta_{as}PO_3$	[33]

Asymmetrical terminal P–O stretching mode: $\upsilon_{as}PO_3$.
Symmetrical terminal P–O stretching mode: $\upsilon_{s}PO_3$.
Asymmetrical terminal P–O bending mode: $\delta_{as}PO_3$.
Symmetrical terminal P–O stretching mode: $\delta_{s}PO_3$.
Asymmetrical bridge P–O stretching mode: $\upsilon_{as}POP$.
Symmetrical bridge P–O stretching mode: $\upsilon_{s}POP$.

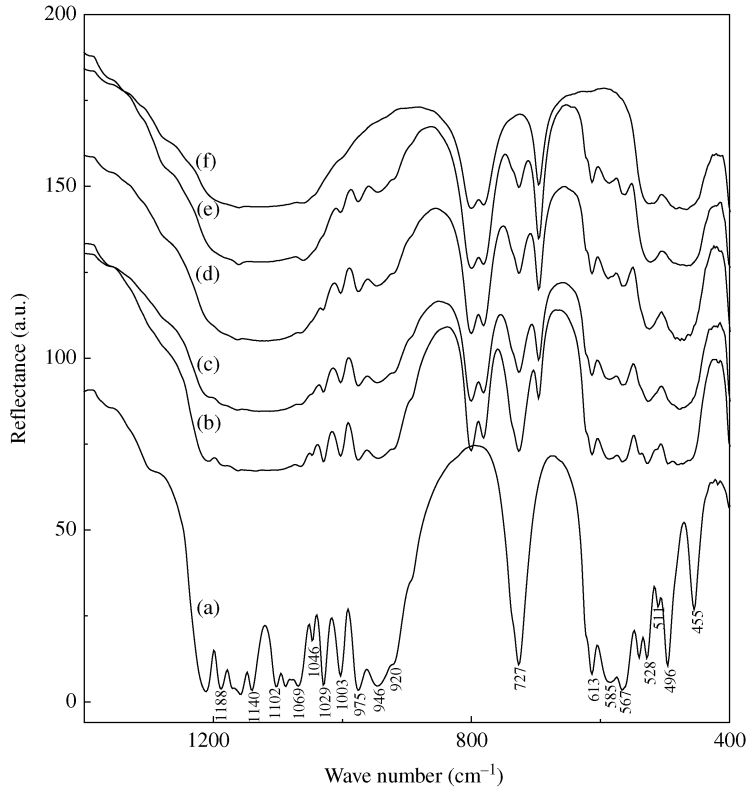

Figure 6 FTIR spectra of the SiO_2–CaP composites thermal-treated at 1000 °C, (a) CaP, (b) 20Si, (c) 40Si, (d) 60Si, (e) 80Si, (f) SiO_2. The intensities of the bands for β-$Ca_2P_2O_7$ at 455, 496, 511, 528, 540, 567, 585, 613, 727, 920, 946, 975, 1003, 1029, 1046, 1054, 1069, 1088, 1102, 1140, 1158, 1170, 1188 cm^{-1} decreased with increasing silica content, whereas, those of the bands for β-quartz at 477, 524, 696, 781, 800, 1063, 1127, 1160 cm^{-1} increased.

TABLE V FTIR absorption bands of the SiO_2–CaP composites sintered at 1000 °C

Wave number (cm^{-1})						Assignments	Ref.
CaP	20Si	40Si	60Si	80Si	SiO_2		
1188	1188					$\upsilon_{as}PO_3(\beta\text{-}Ca_2P_2O_7)$	[33]
1170							
	1162	1162	1162	1161	1160	Si–O–Si asymmetric stretching	[26, 28]
1158						$\upsilon_{as}PO_3(\beta\text{-}Ca_2P_2O_7)$	[33]
1140							
	1127	1127	1127	1127	1127	Si–O–Si asymmetric stretching	[26, 28]
1102						$\upsilon_{as}PO_3(\beta\text{-}Ca_2P_2O_7)$	[33]
1088							
1069	1065	1066	1065	1061	1063	$\upsilon_{as}PO_3(\beta\text{-}Ca_2P_2O_7)$	[33]
						Si–O–Si asymmetric vibrations	[26, 28]
1054						$\upsilon_{s}PO_3(\beta\text{-}Ca_2P_2O_7)$	[33]
1046	1047						
1029	1029	1029	1030				
1003	1003	1003	1003	1003			
975	975	975	975	975		$\upsilon_{as}POP$ ($\beta\text{-}Ca_2P_2O_7$)	[33]
946	945	946	947	946			
920	920	920	920	920			
	801	801	800	800	800	Si–O–Si bending	[33]
	781	781	781	781	781		
727	727	726	726	726		$\upsilon_{s}POP$ ($\beta\text{-}Ca_2P_2O_7$)	[33]
	696	696	696	696	696	Six-membered rings (β-quartz)	[27]
613	613	613	613	613		$\delta_{as}PO_3(\beta\text{-}Ca_2P_2O_7)$	[33]
585	587	586	588	586		$\delta_{s}PO_3(\beta\text{-}Ca_2P_2O_7)$	[33]
567	566	566	566	563		$\delta_{as}PO_3(\beta\text{-}Ca_2P_2O_7)$	[33]
540	539						
528	527	526	524	523	524	$\delta_{as}PO_3(\beta\text{-}Ca_2P_2O_7)$, $\delta_{s}PO_3(\beta\text{-}Ca_2P_2O_7)$	[33]
511	511					Si–O–Si bending	[26, 28]
496	495					$\delta_{s}PO_3(\beta\text{-}Ca_2P_2O_7)$	[33]
	477	477	477	476	477	Si–O–Si bending	[26, 28]
455	455					$\delta_{as}PO_3(\beta\text{-}Ca_2P_2O_7)$	[33]

other hand, the intensities of the vibrational bands characteristics of β-quartz at 474, 521, 695, 781, 800, 1062 cm^{-1} increased with the increase of Si content. For the SiO_2–CaP composites, the bands for $\gamma\text{-}Ca_2P_2O_7$ at 1035, 1080, 1144, 1165, 1187 cm^{-1} overlapped with the broad band of Si–O–Si asymmetric stretching mode at

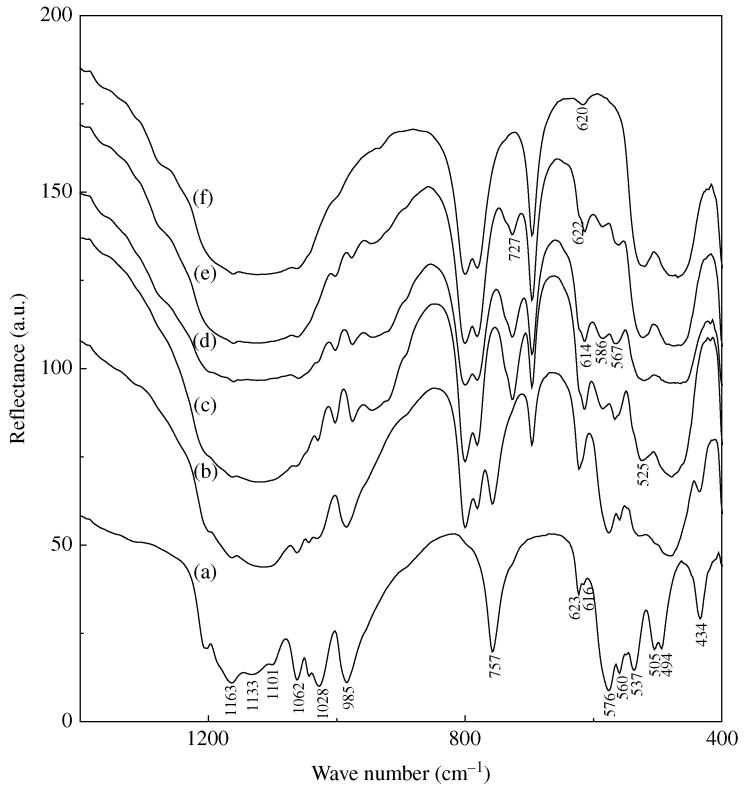

Figure 7 FTIR spectra of the SiO_2–CaP composites thermal-treated at 1200 °C, (a) CaP, (b) 20Si, (c) 40Si, (d) 60Si, (e) 80Si, (f) SiO_2. The vibration bands for $\alpha\text{-}Ca_2P_2O_7$ presented at 434, 494, 505, 537, 560, 576, 616, 623, 757, 985, 1028, 1043, 1062, 1101, 1133, 1163 cm^{-1}, which decreased in intensity in the 20Si composite. In the 40Si composite, the bands for $\beta\text{-}Ca_2P_2O_7$ appeared. For all the SiO_2–CaP composites, the characteristic band of α-cristobalite appeared at about 622 cm^{-1}.

TABLE VI FTIR absorption bands of the SiO_2–CaP composites sintered at 1200 °C

Wave number (cm^{-1})						Assignments	Ref.
CaP	20Si	40Si	60Si	80Si	SiO_2		
1163	1163	1162	1161	1161	1161	$\upsilon_{as}PO_3(\alpha\text{-}Ca_2P_2O_7)$	[26, 28]
						Si–O–Si asymmetric stretching	
1133						$\upsilon_{as}PO_3(\alpha\text{-}Ca_2P_2O_7)$	[31, 33]
	1127	1127	1127	1127	1127	Si–O–Si asymmetric stretching	[26, 28]
1101						$\upsilon_{as}PO_3(\alpha\text{-}Ca_2P_2O_7)$	[31, 33]
1062	1062	1062	1060	1062	1063	$\upsilon_{as}PO_3(\alpha\text{-}Ca_2P_2O_7)$	[31, 33]
						Si–O–Si asymmetric stretching	[26, 28]
1043	1044					$\upsilon_{s}PO_3(\alpha\text{-}Ca_2P_2O_7)$	[31, 33]
1028	1031	1030	1030				
		1003	1003	1003		$\upsilon_{s}PO_3(\beta\text{-}Ca_2P_2O_7)$	[33]
985	985					$\upsilon_{as}POP$ $(\alpha\text{-}Ca_2P_2O_7)$	[31, 33]
		976	976	977		$\upsilon_{as}POP$ $(\beta\text{-}Ca_2P_2O_7)$	[33]
		945	944	946			
		920	920	920			
	800	800	800	800	800	Si–O–Si bending	[27]
	781	781	781	781	781		
757	757					$\upsilon_{s}POP$ $(\alpha\text{-}Ca_2P_2O_7)$	[31, 33]
		726	727	727		$\upsilon_{s}POP$ $(\beta\text{-}Ca_2P_2O_7)$	[33]
	696	696	696	696	696	Six-membered rings (β-quartz)	[27]
623						$\delta_{as}PO_3(\alpha\text{-}Ca_2P_2O_7)$	[31, 33]
	622	622	622	622	620	Six-membered rings (α-cristobalite)	[27]
616						$\delta_{as}PO_3(\alpha\text{-}Ca_2P_2O_7)$	[31, 33]
		614	614	614		$\delta_{as}PO_3(\beta\text{-}Ca_2P_2O_7)$	[33]
		586	585	586		$\delta_{s}PO_3(\beta\text{-}Ca_2P_2O_7)$	[33]
576	576					$\delta_{as}PO_3(\alpha\text{-}Ca_2P_2O_7)$	[31, 33]
		567	565	561		$\delta_{as}PO_3(\beta\text{-}Ca_2P_2O_7)$	[33]
560	560					$\delta_{as}PO_3(\alpha\text{-}Ca_2P_2O_7)$	[33, 34]
537	530						
		525	521	523	521	$\delta_{as}PO_3$, $\delta_{s}PO_3(\beta\text{-}Ca_2P_2O_7)$	[33, 34]
						Si–O–Si bending	
505	505					$\delta_{s}PO_3(\alpha\text{-}Ca_2P_2O_7)$	[33, 34]
494	494						
	477	479	475	476	476	Si–O–Si bending	[26, 28]
434	434					$\delta_{as}PO_3(\alpha\text{-}Ca_2P_2O_7)$	[33]

1000–1300 cm^{-1}. The bands for $\gamma\text{-}Ca_2P_2O_7$ at 451, 498 and 536 cm^{-1} overlapped with the band at 510–540 cm^{-1} and 450–510 cm^{-1} for the Si–O–Si bending modes, respectively. Except for the peaks characteristic of $\gamma\text{-}Ca_2P_2O_7$ and β-quartz, no extra peaks were found in the SiO_2–CaP composite spectra.

The FTIR spectra of the SiO_2–CaP composites sintered at 1000 °C are shown in Fig. 6 and the assignments of the spectra are given in Table V. FTIR bands typical for $\beta\text{-}Ca_2P_2O_7$ could be clearly identified. The peaks for $\beta\text{-}Ca_2P_2O_7$ decreased gradually with the increase in Si content, while the peaks due to β-quartz increased gradually. The FTIR spectra of the SiO_2–CaP composite sintered at 1200 °C are shown in Fig. 7 and the assignments of the spectra are given in Table VI. Since XRD results showed that the main CaP phase for the 20Si composition sintered at 1200 °C was $\alpha\text{-}Ca_2P_2O_7$, all the bands in the corresponding FTIR spectra should be attributed to this phase. Compared to the FTIR spectrum of pure $\alpha\text{-}Ca_2P_2O_7$ (Fig. 7(a)), the peaks for $\alpha\text{-}Ca_2P_2O_7$ decreased in intensity in the composite with 20 wt % silica, some weak peaks even disappeared; on the other hand, the bands for SiO_2 (including β-quartz and α-crystobalite) appeared. For 40Si, 60Si, and 80Si composites, peaks corresponding to $\beta\text{-}Ca_2P_2O_7$ appeared at 556, 593, 986, 1017, 1073, 1135, 1187 cm^{-1}, these results maintained a consistency with XRD results.

4. Discussion

The crystallization and phase transformation in the silica–calcium phosphate composites were dependent on the treatment temperature and chemical composition. In the temperature range 800–1000 °C silica and calcium phosphate components, in the SiO_2–CaP composites, appeared to crystallize independently without any modifications in the crystallization behavior. However, at 1200 °C the presence of calcium phosphate enhanced the crystallization of α-crystobalite. On the other hand, $\beta\text{-}Ca_2P_2O_7$ was stabilized in the presence of silica. The results suggested that these modifications in the crystallization behavior could be attributed to silicate–phosphate ion substitution in these phases.

XRD analyses of the starting material suggested that as the thermal treatment temperature increased, phase transformation of pure $CaHPO_4$ proceeded according to the following equation:

$$CaHPO_4 \xrightarrow{800\,^\circ C} \gamma\text{-}Ca_2P_2O_7 \xrightarrow{1000\,^\circ C} \beta\text{-}Ca_2P_2O_7 \xrightarrow{1200\,^\circ C} \alpha\text{-}Ca_2P_2O_7$$

Data in the literature showed that the $\gamma\text{-}Ca_2P_2O_7 \rightarrow \beta\text{-}Ca_2P_2O_7$ transformation temperature was significantly lower (below 750 °C) than that recorded in the above equation [35, 36]. On the other

hand, the transition from β-$Ca_2P_2O_7$ → α-$Ca_2P_2O_7$ was not significantly different from data in the literature which reported this transformation to take place over a narrow temperature range (1171–1179 °C) [37]. The transformation β-$Ca_2P_2O_7$ → α-$Ca_2P_2O_7$ was accompanied by a decrease in the number of P–O–P asymmetric stretching bands in the FTIR spectra (Figs. 6 and 7). This variation in the number of P–O–P bands is due to the fact that β-$Ca_2P_2O_7$ structure has two P–O–P angles, 131° and 138° [23], while α-$Ca_2P_2O_7$ has only one P–O–P angle of 130° [38], so it is not difficult to understand that the former had more vibration degrees of freedom than the latter compound. Moreover, because the P–O–P bond length in β-$Ca_2P_2O_7$ (1.615 Å) is larger than that in α-$Ca_2P_2O_7$ (1.60 Å), the P–O–P symmetric (975 cm^{-1}) and asymmetric stretching (727 cm^{-1}) vibrations of β-$Ca_2P_2O_7$ were at lower wave numbers than those of the α-$Ca_2P_2O_7$ which appeared at 985 and 757 cm^{-1}, respectively. The vibrations of the terminal P–O bonds are more complicated than P–O–P due to the multiple bond lengths of the former bond. The terminal P–O bond length has five values in α-$Ca_2P_2O_7$ and 10 values in β-$Ca_2P_2O_7$, although the average values are almost the same for these two calcium pyrophosphates. Therefore, it is difficult to make a comparison between α- and β-$Ca_2P_2O_7$ in terms of the vibrational modes of the terminal P–O bond. The accurate crystal structure of γ-$Ca_2P_2O_7$ is still unknown, so it is hard to interpret its FTIR spectrum.

XRD analyses indicated that β-quartz was the dominating silica phase after thermal treatment of pure silica in the temperature range 800–1200 °C. In addition, a small peak at 21.62° could be identified in the XRD spectrum of SiO_2 thermal treated at 1200 °C which indicated traces of α-cristobalite. On the other hand, FTIR analyses showed that the stretching vibration bands of non-bridging oxygen ($Si–O^-$) at 915 and 944 cm^{-1} of the original silica powder almost disappeared after thermal treatment at 800 °C or higher. The disappearance of these FTIR bands was mainly caused by the atomic diffusion at high temperatures. Another important modification in the FTIR spectrum of pure silica was the very obvious small band at about 620 cm^{-1} which appeared only after sintering at 1200 °C (Fig. 8). This band could be caused by the vibration of the six-membered rings in the α-cristobalite structure [27]. In addition, the FTIR spectra of thermally treated and untreated SiO_2 showed a characteristic doublet of the quartz in the range 700–800 cm^{-1}. Data in the literature suggested that this doublet could originate from Si–O–Si bending vibrations due to the different bond angles in the silicooxygen ring [27]. Other reports had assigned these peaks to the symmetric stretching vibration of Si–O–Si or O–Si–O [28, 39].

XRD analyses of SiO_2–CaP composites showed that at 1200 °C, the form of the CaP crystalline phase was dependent on the initial silica concentration. While α-$Ca_2P_2O_7$ crystallized in 20Si, β-$Ca_2P_2O_7$ was formed in 40Si, 60Si, and 80Si. Previous studies in the literature reported the formation of $Ca_3(PO_4)_2SiO_4$ after thermal treatment of HA–silica composite at 1100 °C [25]. However, in our study, no calcium phosphate silicates were detected in the SiO_2–CaP composites even though

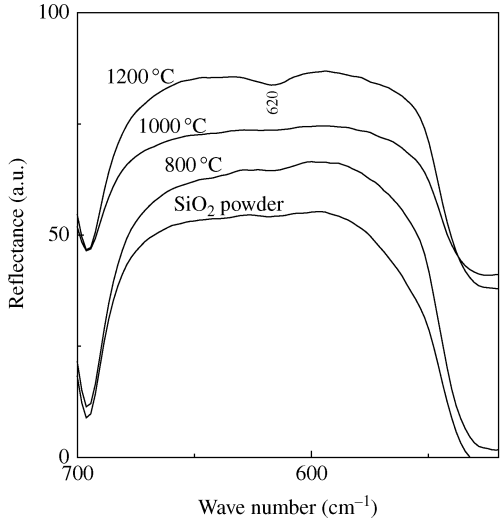

Figure 8 FTIR spectra of SiO_2 sintered at different temperatures. The characteristic band of α-cristobalite at 620 cm^{-1} only presented in the spectrum of SiO_2 thermal-treated at 1200 °C.

we employed a higher treatment temperature for the same dwell time as in Ref. [25]. The difference in the crystallization behavior is due to the dissimilarity in the chemistry of the reactants. The stabilization of β-$Ca_2P_2O_7$ and the enhanced crystallization of α-cristobalite in the SiO_2–CaP composites indicated impurity inclusions and formation of solid solutions during the course of crystallization of these phases. Indeed, compared to the standard PDF card #09-0346, the diffraction peaks of β-$Ca_2P_2O_7$ slightly moved to higher 2θ value, suggesting that silicon atoms substituted some of the phosphorus atoms in the structure of β-$Ca_2P_2O_7$ (Fig. 3(a)). Moreover, compared to PDF card #39-1425, the position of the XRD signals of α-cristobalite in the SiO_2–CaP composites were shifted to lower 2θ values (Fig. 3(b)), implying an increase in the crystal lattice parameters due to incorporation of phosphorus ions in the structure of α-cristobalite. The shift in the 2θ value decreased with decreasing the silica content in the order (80Si > 60Si > 40Si) (Fig. 3(a)), which implied that a dispersive distribution of the calcium phosphate among the silica-rich medium was supportive for phosphorus–silicon substitution. However, the shift in the 2θ value for 20Si was higher than that for 40Si which could be related to the presence of the α-$Ca_2P_2O_7$ in the former sample instead of β-$Ca_2P_2O_7$.

FTIR analyses confirmed the transformation of β-quartz into α-cristobalite, in 20Si sintered at 1200 °C as indicated by the appearance of a band at 622 cm^{-1} characteristic of the latter phase (Fig. 7). The band at 622 cm^{-1} appeared as a shoulder in the FTIR spectra of samples that have higher silica content most probably due to the overlap between this band and the asymmetric P–O bending vibration band at 613 cm^{-1} characteristic of β-$Ca_2P_2O_7$. Except for the 622 cm^{-1} band, all other characteristic FTIR vibrational bands of the silica phases were similar most probably due to the similarity in the Si–O bond lengths and Si–O–Si bond angles in α-cristobalite (1.605 Å, 146.8°) and β-quartz (1.609 Å, 143.7°) [40].

5. Conclusions

Phase transformations of silica and CaP were dependent on the chemical composition and sintering temperature. At 1200 °C, CaP enhanced the transformation of β-quartz to α-cristobalite. In addition, silica stabilized β-$Ca_2P_2O_7$. These modifications in the crystallization behavior are due to silicate–phosphate ion substitution. On the other hand, at lower temperatures (800 and 1000 °C) CaP and silica did not modify their corresponding crystallization behavior.

References

1. W. P. CAO and L. L. HENCH, *Ceram. Inter.* **22** (1996) 493.
2. J. S. SUN, Y. H. TSUANG, C. J. LIAO, H. C. LIU, Y. S. HUANG and F. H. LIN, *J. Biomed. Mater. Res.* **37** (1997) 324.
3. T. KASUGA, M. SAWADA, M. NOGAMI and Y. ABE, *Biomaterials* **20** (1999) 1415.
4. R. L. LEGEROS and J. P. LEGEROS, *Key Eng. Mater.* **240–242** (2003) 3.
5. J. H. LEE, D. H. LEE, H. S. RYU, B. S. CHANG, K. S. HONG and C. K. LEE, *ibid.* **240–242** (2003) 399.
6. S. R. RADIN and P. DUCHEYNE, *J. Biomed. Mater. Res.* **27** (1993) 35.
7. N. KIVRAK and A. C. TAS, *J. Am. Ceram. Soc.* **81** (1998) 2245.
8. L. L. HENCH, *Mater. Sci. Forum* **293** (1999) 37.
9. L. L. HENCH and J. WILSON, *Science* **226** (1984) 630.
10. L. L. HENCH, *J. Am. Ceram. Soc.* **74** (1991) 1487.
11. T. KOKUBO, *J. Non-Cryst. Solids.* **121** (1989) 138.
12. T. KOKUBO, H. M. KIM and M. KAWASHITA, *Biomaterials* **24** (2003) 2161.
13. E. M. CARLISLE, *Science* **167** (1970) 279.
14. A. J. RUYS, *J. Aust. Ceram. Soc.* **29** (1993) 71.
15. Y. TANIZAWA and T. SUZUKI, *Phosphorus Res. Bull.* **4** (1994) 83.
16. K. SUGIYAMA, T. SUZUKI and T. SATOH, *J. Antibact. Antifung. Agents* **23** (1995) 67.
17. L. BOYER, J. CARPENA and J. L. LACOUT, *Solid State Ionics* **95** (1997) 121.
18. I. R. GIBSON, S. M. BEST and W. BONFIELD, *J. Biomed. Mater. Res.* **44** (1999) 422.
19. P. A. A. P. MARQUES, M. C. F. MAGALHAES, R. N. CORREIA and M. VALLET-REGI, *Key Eng. Mater.* **192–195** (2001) 247.
20. S. R. KIM, D. H. RIU, Y. J. LEE and Y. H. KIM, *ibid.* **218–220** (2002) 85.
21. I. R. GIBSON, K. A. HING, S. M. BEST and W. BONFIELD, in ''Proceeding of the 12th International Symposium on Ceramics in Medicine, Japan, November 1999'', edited by H. Ohgushi, G. W. Hastings and T. Yoshikawa (World Scientific Publishing Co Ltd, London, 1999) p. 191.
22. N. PATEL, S. M. BEST, W. BONFIELD, I. R. GIBSON, K. A. HING, E. DAMIEN and P. A. REVELL, *J. Mater. Sci.: Mater. Med.* **13** (2002) 1199.
23. N. C. WEBB, *Acta Cryst.* **21** (1966) 942.
24. A. I. VILLACAMPA and J. M. GARCIA-RUIZ, *J. Cryst. Growth* **211** (2000) 111.
25. L. BERZINA, R. CIMDINS, D. VEMPERE and I. KNETS, *Key Eng. Mater.* **206–213** (2002) 1587.
26. H. A. ELBATAL, M. A. AZOOZ, E. M. A. KHALIL, A. S. MONEM and Y. M. HAMDY, *Mater. Chem. Phys.* **80** (2003) 599.
27. M. SITARZ, M. HANDKE and W. MOZGAWA, *Spectrochimica Acta* **56A** (2000) 1819.
28. Z. WU, K. LEE, Y. LIN, X. LAN and L. HUANG, *J. Non-cryst. Solid* **320** (2003) 168.
29. J. XU, I. S. BUTLER and D. F. R. GILSON, *Spectrochimica Acta* **55A** (1999) 2801.
30. L. TORTET, J. R. GAVARRI, G. NIHOUL and A. J. DIANOUX, *J. Solid State Chem.* **132** (1997) 6.
31. B. C. CORNILSEN and R. A. CONDRATE, *J. Inorg. Nucl. Chem.* **41** (1979) 602.
32. B. O. FOWLER, E. C. MORENO and W. E. BROWN, *Arch. Oral. Biol.* **11** (1966) 477.
33. V. VINCENT, C. BREANDON, G. NIHOUL and J. R. GAVARRI, *Eur. J. Solid State Inorg. Chem.* **34** (1997) 571.
34. V. P. M. PILLAI, B. R. THOMAS, V. U. NAYAR and K. H. LII, *Spectrochimica Acta* **55A** (1999) 1809.
35. E. J. FOX and K. G. CLARK, *Ind. Eng. Chem.* **35** (1943) 1264.
36. A. O. MCINTOSH and W. L. JABLONSKI, *Anal. Chem.* **28** (1956) 1424.
37. J. A. PARODI, R. L. HICKOK, W. G. SEGELKEM and J. R. COOPER, *J. Electrochem. Soc.* **112** (1965) 688.
38. C. CALVO, *Inorg. Chem.* **7** (1968) 1345.
39. S. M. ABO-NAF, F. H. ELBATAL and M. A. AZOOZ, *Mater. Chem. Phys.* **77** (2002) 846.
40. E. GORLICH, *Ceram. Inter.* **8** (1982) 3.

Received 25 November 2003
and accepted 27 April 2004